Rare Met. (2020) 39(9):1063–1071
https://doi.org/10.1007/s12598-020-01462-w

RARE METALS
www.editorialmanager.com/rmet

In situ sol–gel synthesis of $Ti_2Nb_{10}O_{29}$/C nanoparticles with enhanced pseudocapacitive contribution for a high-rate lithium-ion battery

Guang-Yin Liu, Yi-Yang Zhao, Yu-Feng Tang, Xiao-Di Liu*, Miao Liu, Peng-Jiang Wu

Received: 18 December 2019 / Revised: 18 February 2020 / Accepted: 18 May 2020 / Published online: 23 June 2020
© The Nonferrous Metals Society of China and Springer-Verlag GmbH Germany, part of Springer Nature 2020

Abstract $Ti_2Nb_{10}O_{29}$/C nanoparticles with a carbon content of 13 wt% and a mean size of 50 nm were fabricated through a convenient and effective in situ sol–gel process. The small grain size and carbon modification can improve the pseudocapacitive effect of the $Ti_2Nb_{10}O_{29}$/C nanoparticles, leading to excellent rate capacity, especially at high current rate. Specifically, the discharge capacity of the $Ti_2Nb_{10}O_{29}$/C electrode is 258.3, 236.0, 216.6, 184.5 and 161.5 mAh·g^{-1} at different current densities of 1C, 5C, 10C, 20C and 30C. Nevertheless, the discharge capacity of the $Ti_2Nb_{10}O_{29}$ electrode is 244.9 mAh·g^{-1} at 1C, which is rapidly reduced to 89.7 mAh·g^{-1} at 30C. In addition, the small size and carbon layer of the $Ti_2Nb_{10}O_{29}$/C nanoparticles can supply abundant active sites for Li^+ storage as well as enhance the electronic conductivity and Li^+ diffusion, endowing these nanoparticles with a high discharge capacity and excellent cycle performance.

Keywords Nanoparticles; Anode materials; Sol–gel method; Energy storage

1 Introduction

Lithium-ion batteries (LIBs) are vitally important electrochemical power sources for electric vehicles and hybrid electric vehicles (EVs/HEVs) [1]. Owing to the rapid development of EVs/HEVs, it is very necessary to exploit LIBs with high energy density, good rate capacity and high security. It is well known that the properties of the anodes are significant for the performance of LIBs. Graphite is widely used as an anodic material in the commercial LIBs; nevertheless, its relatively low working potential (~ 0.1 V vs. Li^+/Li) can lead to the generation of Li dendrites, especially at high current density [2, 3]. Thus, in term of safety, graphite is not very suitable for using as anode materials in LIBs for EVs/HEVs. Accordingly, there is a great interest in exploring alternative anode materials with good safety performance and high discharge capacity. Currently, $Ti_2Nb_{10}O_{29}$ is considered to be a promising anode for LIBs due to its large theoretical capacity (396 mAh·g^{-1}) and high working potential (~ 1.7 V vs. Li^+/Li), which is beneficial for achieving high energy density and improved safety [4]. Moreover, $Ti_2Nb_{10}O_{29}$ has a stable Wadsley–Roth shear structure consisting of $4 \times 3 \times \infty$ ReO_3-type blocks, leading to excellent cycle stability [5]. Therefore, $Ti_2Nb_{10}O_{29}$ has attracted tremendous research interests among the LIBs fields for EVs/HEVs.

Nevertheless, $Ti_2Nb_{10}O_{29}$ has a low Li^+ diffusion coefficient, which can lead to poor rate ability and accordingly severely hinder its practical application in EVs/HEVs [6]. Recently, the construction of nanostructured anodes has been used for solving the problem of slow diffusion of Li^+ [7–10]. More importantly, it has been proved that the surface-controlled pseudocapacitive effect can replace the diffusion-controlled Li^+ insertion process at high current rates, resulting in outstanding rate capability [10–14]. The smaller the size of the anode is, the higher the number of electrically charged species is on the anode surface–subsurface, which benefits charge storage via the

Electronic supplementary material The online version of this article (https://doi.org/10.1007/s12598-020-01462-w) contains supplementary material, which is available to authorized users.

G.-Y. Liu, Y.-Y. Zhao, Y.-F. Tang, X.-D. Liu*, M. Liu, P.-J. Wu
College of Chemistry and Pharmaceutical Engineering, Nanyang Normal University, Nanyang 473061, China
e-mail: liuxiaodiny@126.com

pseudocapacitive effect and accordingly enhances the rate capacity [14]. Therefore, decreasing the size of the anode is a fairly promising direction for the construction of anodic materials with high energy density. Some $Ti_2Nb_{10}O_{29}$ micro-/nanostructures have already been reported [15–18]; nevertheless, most of these materials are prepared at high temperature for prolonged periods, which generally leads to a large particle size and small surface area. Hence, there is still broad space to develop facile methods to prepare $Ti_2Nb_{10}O_{29}$ nanomaterials with smaller size and larger specific surface area.

On the other hand, Ti^{4+} ($3s^23p^6$) and Nb^{5+} ($4s^24p^6$) in $Ti_2Nb_{10}O_{29}$ do not have single electron, and thus, $Ti_2Nb_{10}O_{29}$ possesses a low intrinsic electronic conductivity, which also negatively affects its rate capability. Fortunately, carbon coating has been demonstrated to be a valid strategy for improving the electronic conductivity of anode materials [19–21]. Nevertheless, studies for the carbon coating of $Ti_2Nb_{10}O_{29}$ have been rarely reported [22–24]. In addition, the coating techniques that are frequently used usually require multiple steps, and post-carbon modification processes are not beneficial for the uniform coating of carbon on every nanoparticle [20, 25]. Thus, it is essential to explore facile methods for the direct in situ carbonization of $Ti_2Nb_{10}O_{29}$.

Herein, in consideration of both the "nanosize" and "carbon coating," a convenient and effective in situ sol–gel method is employed to prepare carbon-coated $Ti_2Nb_{10}O_{29}$ nanoparticles. The as-obtained $Ti_2Nb_{10}O_{29}$/C nanoparticles have a small size (average particle size of $\sim$ 50 nm) and an extremely large specific surface area (186.8 $m^2 \cdot g^{-1}$); moreover, carbon is uniformly coated onto the surfaces of the $Ti_2Nb_{10}O_{29}$ nanoparticles. The synergistic effect between reduced particle size and uniform carbon coating can not only improve the reaction kinetics of the $Ti_2Nb_{10}O_{29}$/C nanoparticles but also remarkably enhance their pseudocapacitive effect, endowing them with superior electrochemical properties, especially rate performance.

2 Experimental

First, 3 g P123 ($EO_{20}PO_{70}EO_{20}$) was added into 100 ml ethanol under vigorous stirring for 5 min. Then, 5 mmol $NbCl_5$ and 1 mmol $Ti(OC_3H_7)_4$ were added into the above solution and the mixture was stirred at 80 °C for 1 h to form a sol; the sol was then dried at 100 °C for 2 h in vacuum to generate a gel. Finally, $Ti_2Nb_{10}O_{29}$/C nanoparticles with a black color were prepared by calcining the gel at 850 °C for 8 h in N_2 atmosphere. For comparison, $Ti_2Nb_{10}O_{29}$ nanoparticles with white color were synthesized using the same processes except that the gel was calcined in an air atmosphere.

The morphologies, structures and electrochemical performance of the products were studied by using multiple characterization techniques: X-ray diffraction (XRD), field emission scanning electron microscopy (FESEM), transmission electron microscope (TEM), high-resolution transmission electron microscope (HRTEM), X-ray photoelectron spectroscopy (XPS), Raman spectroscopy (RS), Brunauer–Emmett–Teller adsorption isotherm (BET), thermogravimetric analysis (TG), cyclic voltammetry (CV) and electrochemical impedance spectroscopy (EIS). The corresponding instruments and methods used are shown in the Supporting Information.

3 Results and discussion

The sizes and nanostructures of the obtained $Ti_2Nb_{10}O_{29}$/C and $Ti_2Nb_{10}O_{29}$ nanoparticles were characterized by TEM, HRTEM and SEM. As shown in TEM images (Fig. 1a, c), the mean size of the $Ti_2Nb_{10}O_{29}$/C nanoparticles is much smaller than that of the $Ti_2Nb_{10}O_{29}$ nanoparticles (50 vs. 200 nm), which can be further confirmed by SEM results (Fig. S1). In addition, the $Ti_2Nb_{10}O_{29}$/C nanoparticles have good monodispersity due to the carbon coating. As shown in the HRTEM images of the $Ti_2Nb_{10}O_{29}$ and $Ti_2Nb_{10}O_{29}$/C nanoparticles (Fig. 1b, d), well-resolved fringes are observed with a lattice spacing of 0.360 nm, which can be assigned to the interplanar distance of the (400) plane for the monoclinic $Ti_2Nb_{10}O_{29}$. It is noteworthy that the surface of the $Ti_2Nb_{10}O_{29}$ nanoparticles is continuously

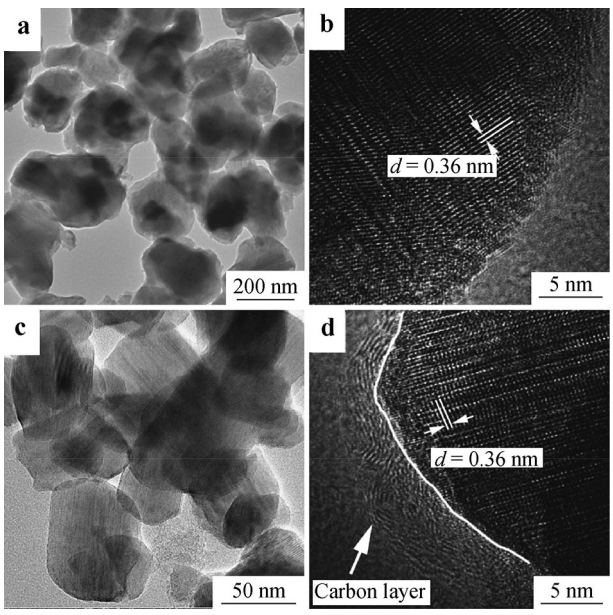

Fig. 1 TEM images of **a** $Ti_2Nb_{10}O_{29}$ nanoparticles and **c** $Ti_2Nb_{10}O_{29}$/C nanoparticles; HRTEM images of **b** $Ti_2Nb_{10}O_{29}$ nanoparticles and **d** $Ti_2Nb_{10}O_{29}$/C nanoparticles

covered by a carbon layer with a thickness of ~ 2 nm (arrowed in Fig. 1d). In addition, carbon coatings do not exhibit any regular lattice fringes, indicating that they are present in an amorphous form. Benefiting from the decreasing grain size and good dispersity, the $Ti_2Nb_{10}O_{29}$/C nanoparticles exhibit an extremely high specific surface area of approximately 186.8 $m^2 \cdot g^{-1}$ (Fig. S2).

The structure of the $Ti_2Nb_{10}O_{29}$/C nanoparticles was firstly characterized by XRD (Fig. 2a). The peaks match very well with the monoclinic-type $Ti_2Nb_{10}O_{29}$ (JCPDS No. 40-0039). Compared to pure $Ti_2Nb_{10}O_{29}$ nanoparticles, no diffraction peaks attributed to crystalline carbon can be found, so the carbon coatings likely exist in anamorphous state. RS (Fig. 2b) can be used to further identify the structure of the carbon layer because the Raman spectra for crystalline and amorphous carbon possess D (disorder or defect) and G (graphite) bands with different intensities and positions [26]. In Fig. 2b, two peaks at wavenumbers of 1333.5 and 1588.1 cm^{-1} agree with the D and G-bands of carbon, respectively. The ratio of the D-band and G-band intensities (I_D/I_G) is ~ 1.23, which convincingly demonstrates that the carbon layer has an amorphous structure [27, 28]; moreover, the high intensity of the D-band reflects a high degree of disorder in the carbon layer, which can effectively improve the electrical conductivity of $Ti_2Nb_{10}O_{29}$ [26, 29].

XPS was used to analyze the chemical states of the samples. The Ti 2p core level spectrum of the $Ti_2Nb_{10}O_{29}$/C nanoparticles (Fig. 3a) is composed of two peaks that can be confirmed as Ti^{4+} ($2p_{3/2}$) and Ti^{4+} ($2p_{1/2}$) at 459.5 and 465.3 eV, respectively [30]; moreover, for the Nb 3d XPS spectrum (Fig. 3b), two peaks at 207.9/210.8 eV can be attributed to Nb $3d_{5/2}$/Nb $3d_{3/2}$, which verifies the existence of Nb in its highest oxidation state of 5+ [31], whereas the Ti 2p and Nb 3d peaks for the $Ti_2Nb_{10}O_{29}$ nanoparticles are clearly shifted toward lower values by 0.8 eV compared to the $Ti_2Nb_{10}O_{29}$/C nanoparticles, which may be caused by the absence of carbon [32]. As depicted in Fig. 3c, the C 1s spectra for $Ti_2Nb_{10}O_{29}$/C and $Ti_2Nb_{10}O_{29}$ all show three peaks. Namely, the dominant peak appearing at 284.8 eV is attributed to C–C, and another two peaks located at 286.0 and 288.3 eV can be assigned to C–O and C=O, respectively [33, 34]. The O 1s spectrum of the $Ti_2Nb_{10}O_{29}$ nanoparticles (Fig. 3d) can be split into two peaks. In contrast, the O 1s spectrum of the $Ti_2Nb_{10}O_{29}$/C nanoparticles is composed of three peaks at 531.1, 532.3 and 533.5 eV, which are due to M–O (M = Nb, Ti), C–O and C=O, respectively [35]. Additionally, based on the results from TG results (Fig. S3), the content of carbon in $Ti_2Nb_{10}O_{29}$/C nanoparticles is confirmed to be 13 wt%.

It is known that the sol–gel process is an important technology for the synthesis of nanomaterials [36–38]. $Ti_2Nb_{10}O_{29}$ precursors with small size can be produced by the sol–gel process under mild reaction conditions (low temperature and short reaction time); moreover, P123 can absorb onto the $Ti_2Nb_{10}O_{29}$ precursors surfaces, which is beneficial to prevent the growth of the precursors [39, 40]. Then, after the calcination of the precursors in an air atmosphere, pure $Ti_2Nb_{10}O_{29}$ nanoparticles are obtained, whereas $Ti_2Nb_{10}O_{29}$ nanoparticles with a uniform carbon layer coating can be easily prepared under an insert atmosphere of N_2. Hence, it is reasonable to conclude that carbon is produced from the pyrolysis of P123. More importantly, carbon coatings can effectively inhibit the further growth and aggregation of nanoparticles in the calcination process, so $Ti_2Nb_{10}O_{29}$/C nanoparticles with small particle size and good dispersity can be obtained [28]. The growth mechanisms for the $Ti_2Nb_{10}O_{29}$/C and $Ti_2Nb_{10}O_{29}$ nanoparticles are illustrated in Fig. 4.

The CV method was used to investigate the electrochemical discharge/charge reactions of the $Ti_2Nb_{10}O_{29}$/C electrode. It can be seen that the CV curve for the first cycle (Fig. 5) exhibits a pair of main redox peaks (1.71/

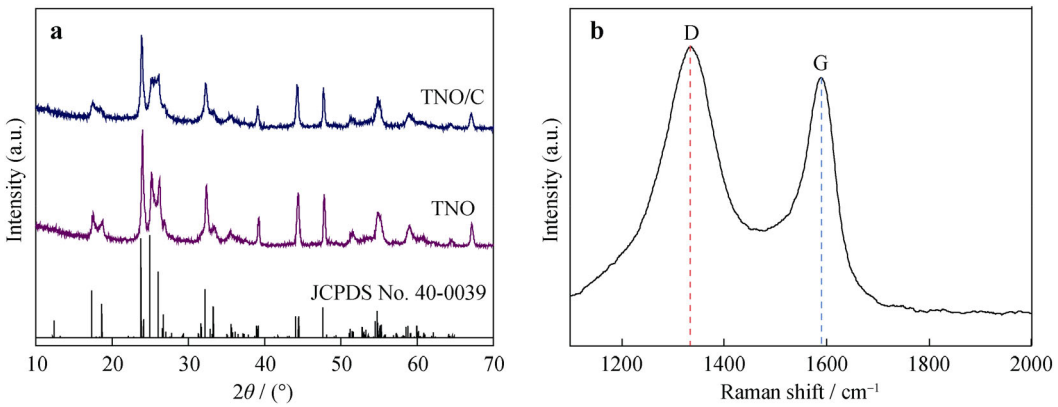

Fig. 2 **a** XRD patterns of $Ti_2Nb_{10}O_{29}$/C nanoparticles (TNO/C) and $Ti_2Nb_{10}O_{29}$ nanoparticles (TNO); **b** Raman spectrum of $Ti_2Nb_{10}O_{29}$/C nanoparticles

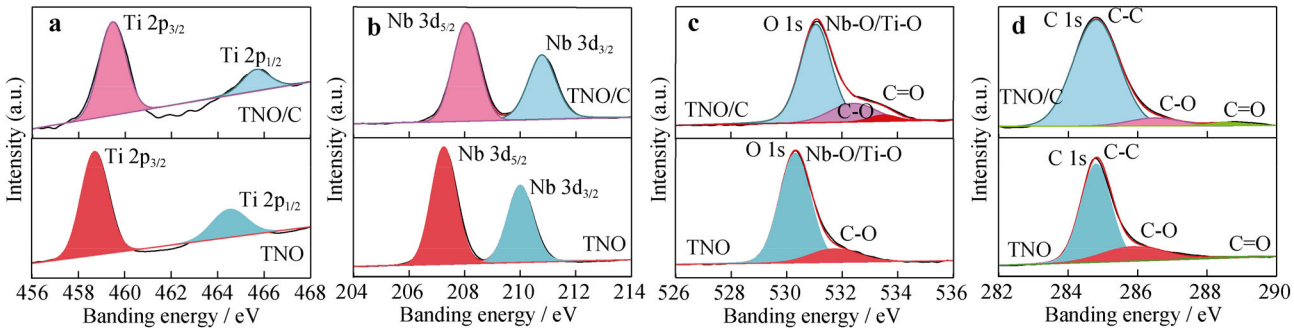

Fig. 3 **a** Ti 2p, **b** Nb 3d, **c** O 1s and **d** C1s XPS spectra of $Ti_2Nb_{10}O_{29}$/C nanoparticles (TNO/C) and $Ti_2Nb_{10}O_{29}$ nanoparticles (TNO)

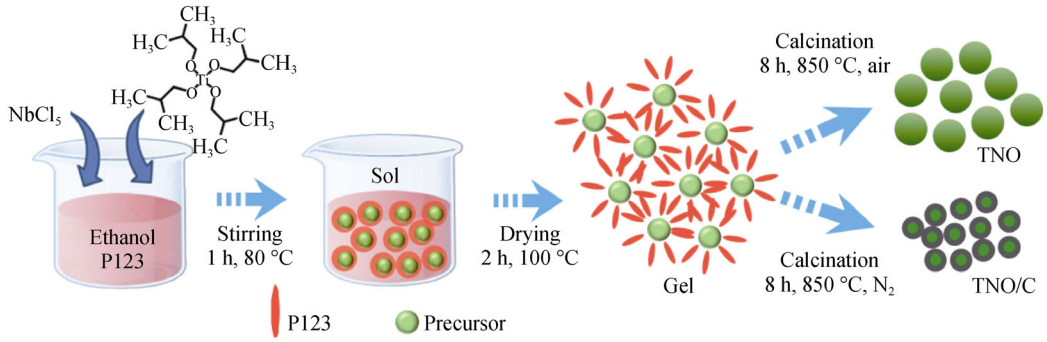

Fig. 4 Growth mechanism of $Ti_2Nb_{10}O_{29}$/C nanoparticles (TNO/C) and $Ti_2Nb_{10}O_{29}$ nanoparticles (TNO)

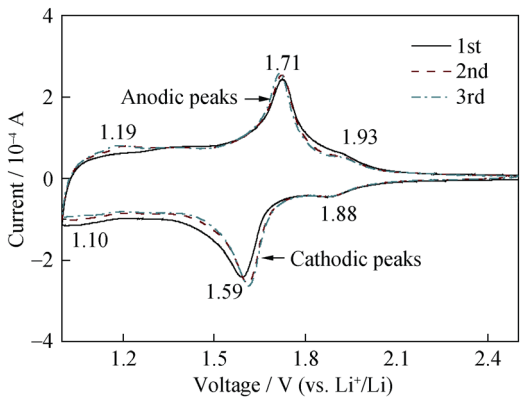

Fig. 5 CV curves of $Ti_2Nb_{10}O_{29}$/C nanoparticles at a scanning rate of 0.1 $mV{\cdot}s^{-1}$ in potential range between 1.0 and 2.5 V (vs. Li^+/Li)

1.59 V) and two pairs of minor redox peaks (1.19/1.10 and 1.93/1.88 V), corresponding to Nb^{5+}/Nb^{4+}, Nb^{4+}/Nb^{3+} and Ti^{4+}/Ti^{3+}, respectively [41]. Hence, $Ti_2Nb_{10}O_{29}$ exhibits a high theoretical capacity due to the three-electron transfer. In the following two cycles, the positions of the three pairs of redox peaks remain almost unchanged, indicating excellent cycling stability, which can be further verified from the corresponding discharge–charge curves (Fig. S4). In addition, according to the major cathodic/anodic peaks, the operating voltage of the $Ti_2Nb_{10}O_{29}$/C electrode is as high as 1.65 V, which can restrain the generation of Li dendrites and accordingly result in a high level of security for the $Ti_2Nb_{10}O_{29}$/C electrode [42].

Figure 6a, b shows the first discharge–charge curves for the two samples at various current rates. With current density increasing, the first discharge capacities for the $Ti_2Nb_{10}O_{29}$/C electrode are slowly reduced from 280.7 to 223.9, 209.4, 175.7 and 151.6 $mAh{\cdot}g^{-1}$. In contrast, the discharge capacities of the $Ti_2Nb_{10}O_{29}$ electrode are greatly reduced; for instance, the discharge capacity is 259.2 $mAh{\cdot}g^{-1}$ at 1C, which is reduced to just 85.9 $mAh{\cdot}g^{-1}$ at a high current density of 30C. The long-term cycling stability of the $Ti_2Nb_{10}O_{29}$/C and $Ti_2Nb_{10}O_{29}$ electrodes for 300 cycles at a current density as high as 10C is shown in Fig. 6c. The $Ti_2Nb_{10}O_{29}$/C electrode exhibits large first discharge/charge capacities of 200.0/198.9 $mAh{\cdot}g^{-1}$ and accordingly possesses a high initial coulombic efficiency (99.5%), which favors stable cycle performance [43]. Actually, after 300 cycles, the discharge capacity of the $Ti_2Nb_{10}O_{29}$/C electrode is maintained at 181.3$mAh{\cdot}g^{-1}$ (90.7% of the first discharge capacity). In contrast, the $Ti_2Nb_{10}O_{29}$ electrode exhibits a lower discharge capacity of 127.6 $mAh{\cdot}g^{-1}$ and a lower capacity retention of 79.3%. The carbon layer modification, small size and large surface area of the $Ti_2Nb_{10}O_{29}$/C nanoparticles can stabilize the structure, reduce Li^+ diffusion paths and supply a large number of active sites; therefore, the $Ti_2Nb_{10}O_{29}$/C electrode has high discharge capacity and

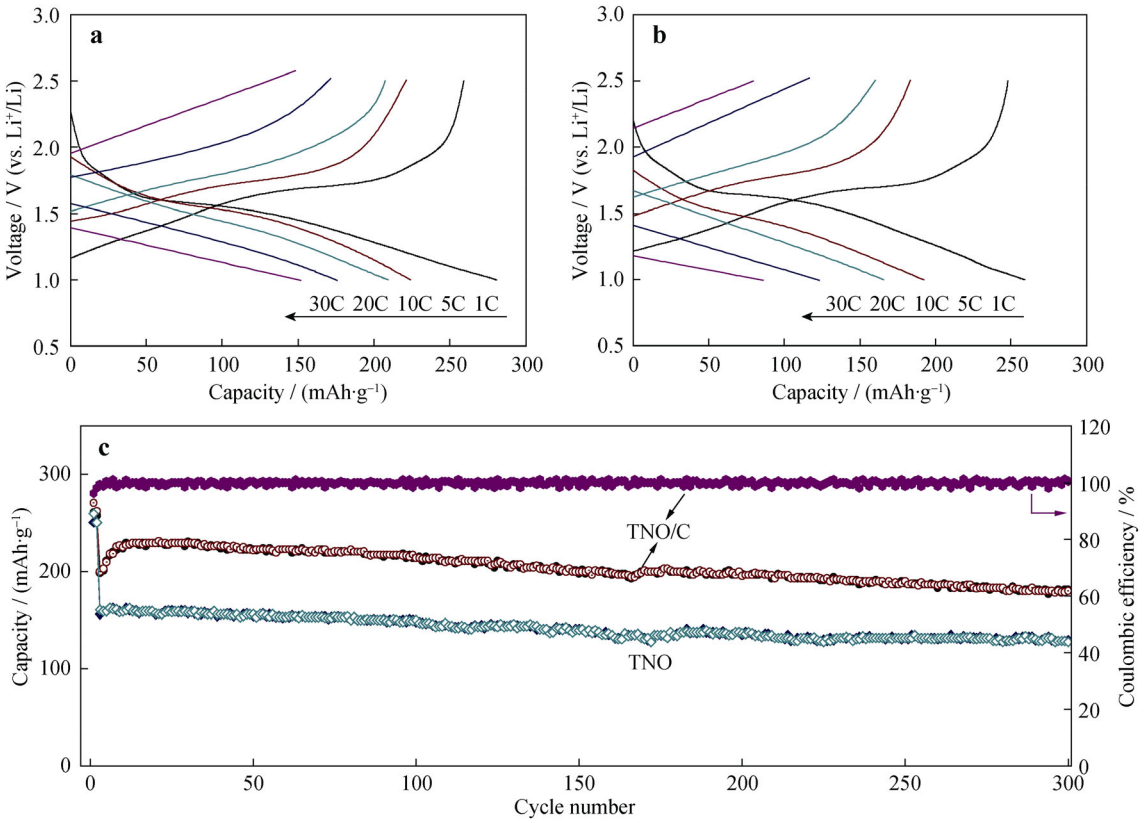

Fig. 6 Initial discharge–charge curves of **a** $Ti_2Nb_{10}O_{29}$/C nanoparticles and **b** $Ti_2Nb_{10}O_{29}$ nanoparticles at 1C, 5C, 10C, 20C and 30C; **c** cycle performance of $Ti_2Nb_{10}O_{29}$/C nanoparticles (TNO/C) and $Ti_2Nb_{10}O_{29}$ nanoparticles (TNO) in voltage range of 1.0-2.5 V at 10C

good cycle performance [44, 45]. In addition, the $Ti_2Nb_{10}O_{29}$/C electrode exhibits a longer activated process than the $Ti_2Nb_{10}O_{29}$ electrode, which may be caused by the insufficient contact of the electrode materials with the electrolyte in the fresh cells [46–48].

The rate capabilities for the two samples are compared, and the results are shown in Fig. 7a. It is clear that, as the current densities are increased from 1C to 5C, 10C, 20C and 30C, the $Ti_2Nb_{10}O_{29}$/C electrode exhibits excellent rate capability with discharge capacities of 258.3, 236.0, 216.6, 184.5, and 161.5 mAh·g^{-1}, respectively, whereas the corresponding value for the $Ti_2Nb_{10}O_{29}$ electrode is 244.9 mAh·g^{-1} (1C), which is greatly reduced to 89.7 mAh·g^{-1} at high current density (30C). Subsequently, as the current density is reduced to 1C, a high discharge capacity of 257.3 mAh·g^{-1} is recovered, suggesting that the $Ti_2Nb_{10}O_{29}$/C electrode has good structural stability. Additionally, compared with other Nb-based electrodes

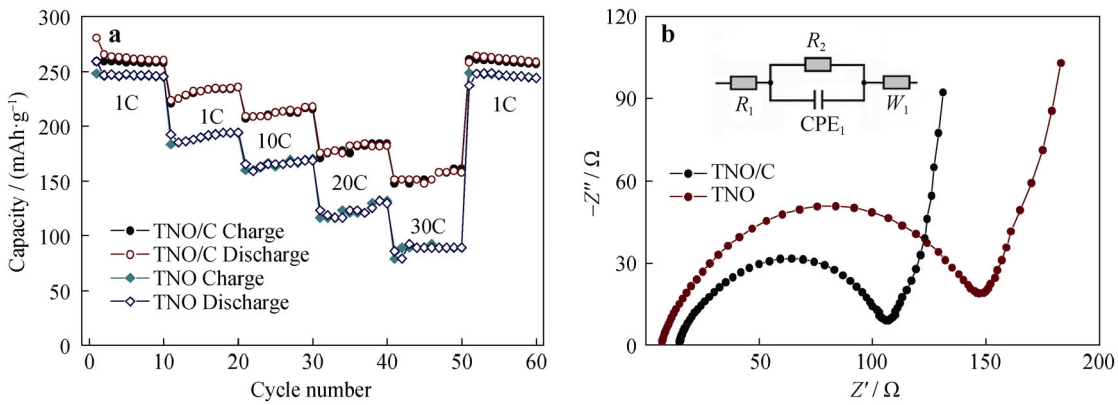

Fig. 7 **a** Rate capacity and **b** Nyquist plots of $Ti_2Nb_{10}O_{29}$/C nanoparticles (TNO/C) and $Ti_2Nb_{10}O_{29}$ nanoparticles (TNO), and inset in **b** being equivalent electrical circuit model

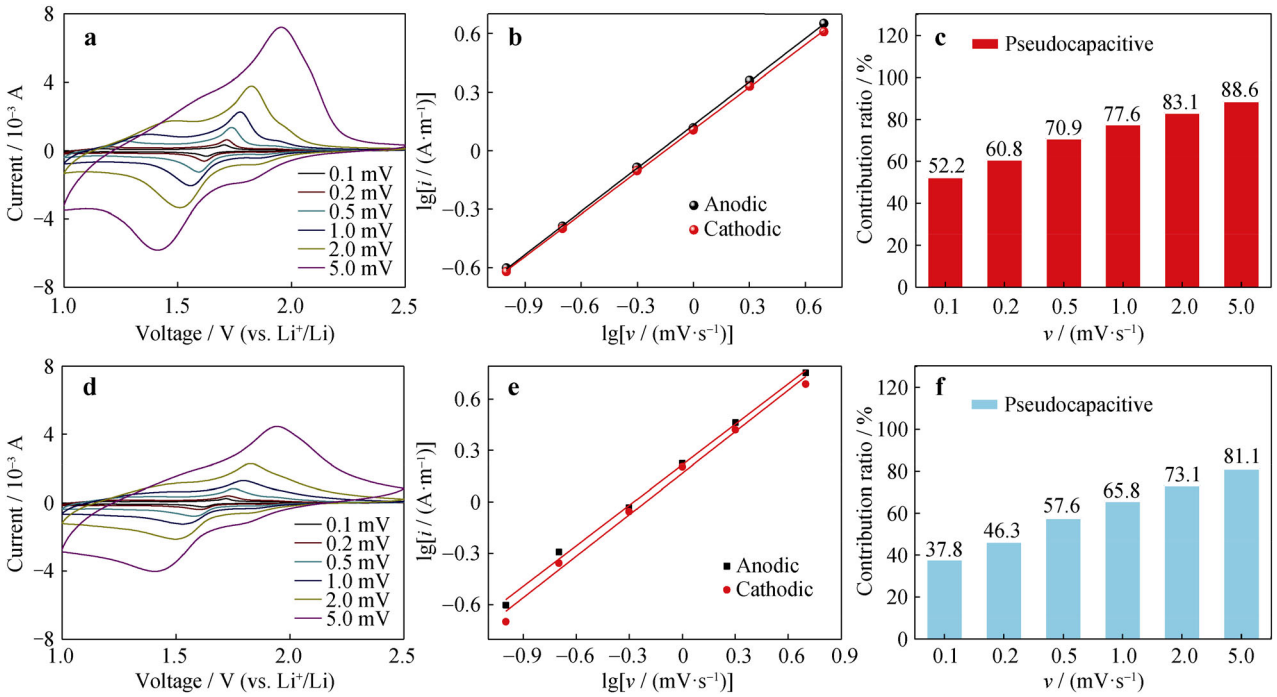

Fig. 8 CV curves of **a** $Ti_2Nb_{10}O_{29}$/C nanoparticles and **d** $Ti_2Nb_{10}O_{29}$ nanoparticles at different scanning rates from 0.1 to 5 $mV{\cdot}s^{-1}$ with potential window of 1.0–2.5 V vs. Li/Li^+; lg*i*-lg*v* plots of **b** $Ti_2Nb_{10}O_{29}$/C nanoparticles and **e** $Ti_2Nb_{10}O_{29}$ nanoparticles; pseudocapacitive and diffusion-controlled contributions of **c** $Ti_2Nb_{10}O_{29}$/C nanoparticles and **f** $Ti_2Nb_{10}O_{29}$ nanoparticles at different scanning rates

(Fig. S5), the $Ti_2Nb_{10}O_{29}$/C electrode possesses outstanding rate capacity.

The electrical conductivity of the $Ti_2Nb_{10}O_{29}$/C electrode can be prominently improved due to the carbon layer, so the rate capability is greatly improved [49]. EIS tests were then performed to further prove the enhancement of the electronic conductivity. The Nyquist plots for the two samples are displayed in Fig. 7b. Both Nyquist plots show semicircles and sloping lines in the high-frequency and low-frequency regions, respectively. The inset in Fig. 7b shows the equivalent circuit model, in which R_1, R_2, W_1 and CPE_1 are the Ohmic resistance of the cell, charge-transfer resistance, Warburg impedance for the Li^+ diffusion resistance in the electrode and constant phase element, respectively. According to the fitted results, the $Ti_2Nb_{10}O_{29}$ electrode possesses a larger R_2 compared to the $Ti_2Nb_{10}O_{29}$/C electrode (83.8 vs. 64.4 Ω), demonstrating that the $Ti_2Nb_{10}O_{29}$/C electrode has good electron and Li-ion transport during cycling due to the carbon coating [9, 50]. In addition, the Li^+-diffusion coefficient (D) for the two samples is further researched based on the following equations [51]:

$$Z' = R_1 + R_2 + \sigma\omega^{-0.5} \quad (1)$$

$$D = (RT)^2/2\left(An^2F^2C\sigma\right)^2 \quad (2)$$

where Z', σ, ω, R, T, A, n, F and C are the real part of the impedance, Warburg factor, angular frequency, gas constant, absolute temperature, surface area, number of electrons transferred in the redox reactions, Faraday constant and concentration of Li^+ in $Ti_2Nb_{10}O_{29}$, respectively. According to the slopes of the Z'-$\omega^{-0.5}$ plots (Fig. S6), $Ti_2Nb_{10}O_{29}$ nanoparticles have a larger σ value than the $Ti_2Nb_{10}O_{29}$/C nanoparticles (294.14 vs. 94.41 $\Omega{\cdot}cm^2{\cdot}s^{-0.5}$). Therefore, based on Eq. (2), the D value for the $Ti_2Nb_{10}O_{29}$ nanoparticles is smaller than that for the $Ti_2Nb_{10}O_{29}$/C nanoparticles, and eventually the kinetics for the lithium-ion and electron transfer in the $Ti_2Nb_{10}O_{29}$/C electrode become faster than that for the $Ti_2Nb_{10}O_{29}$ electrode [52]. In order to get more electrochemical information, EIS measurements of the $Ti_2Nb_{10}O_{29}$/C and $Ti_2Nb_{10}O_{29}$ electrodes after 50 cycles were also carried out, and the results are shown in Fig. S7. As we can see, the $Ti_2Nb_{10}O_{29}$/C/Li cell exhibits a lower R_2 value (110.2 Ω) after 50 cycles compared to the $Ti_2Nb_{10}O_{29}$/Li cell (150.1 Ω), indicating that the carbon layer in $Ti_2Nb_{10}O_{29}$/C has maintained a fairly good electronic conductivity even after 50 cycles. In addition, the enlarged R_2 value of the $Ti_2Nb_{10}O_{29}$/C and $Ti_2Nb_{10}O_{29}$ electrodes after 50 cycles may be attributed to the developed internal resistance upon charge/discharge cycle, which is a common phenomenon observed in the electrodes of Li-ion battery [53].

Additionally, as the size of anode is reduced to nanoscale dimensions, a fairly large amount of stored charges and a fast charge/discharge rate can be easily obtained

[49, 54]. The total stored charges are mainly composed of contributions from the diffusion-controlled Li^+ insertion process and the surface-controlled pseudocapacitance. As the grain size is reduced to the nanoscale regime, pseudocapacitance is important to the total stored charge due to the large number of surface atoms [55]. The contribution of the pseudocapacitive effect can be determined by CV tests conducted at different sweep rates (Fig. 8a, d) on the basis of the following equations [56]:

$$i = av^b \tag{3}$$

$$\lg i = b \times \lg v + \lg a \tag{4}$$

where i and v is the measured current intensity and sweep rate, respectively, and a and b are the appropriate constants. There are two well-defined cases: for $b = 1.0$, i is proportional to v and the process is limited by the pseudocapacitive effect; for $b = 0.5$, i is proportional to $v^{1/2}$ and the electrochemical reaction is controlled by Li^+ diffusion. According to the slopes of lg$i$ vs. lg$v$ plots (Fig. 8b, e), b is equal to 0.847/0.808 and 0.818/0.784, for the middle cathodic and anodic peaks of the two electrodes, respectively, indicating that Li^+ storage reactions of the two electrodes are controlled by two Li^+-storage mechanisms: the Li^+-insertion process and pseudocapacitive effect [57, 58]:

$$i(V) = k_1 v + k_2 v^{1/2} \tag{5}$$

$$i(V)/v^{1/2} = k_1 v^{1/2} + k_2 \tag{6}$$

where $i(V)$ is the total current response, k_1 and k_2 are adjustable parameters, and $k_1 v$ and $k_2 v^{1/2}$ are the current contributions from the surface-controlled pseudocapacitive effect and diffusion-controlled Li^+ insertion process, respectively. Based on Eq. (6), k_1 and k_2 correspond to the slope and intercept of the plot of $i(V)/v^{1/2}$ vs. $v^{1/2}$. As shown in Fig. 8c, $k_1 v$ at specific scan rates can be calculated to be 52.2%, 60.8%, 70.9%, 77.6%, 83.1% and 88.6%, respectively. Obviously, $k_1 v$ is gradually enlarged with scan rate increasing, indicating that the total stored charge for the $Ti_2Nb_{10}O_{29}$/C electrode is mostly controlled by the pseudocapacitive process at high sweep rates. For comparison, the pseudocapacitive contributions for the $Ti_2Nb_{10}O_{29}$ electrode at various scan rates were also studied, and it was found that the $Ti_2Nb_{10}O_{29}$ electrode possesses smaller pseudocapacitive contributions compared to the $Ti_2Nb_{10}O_{29}$/C electrode (Fig. 8f). Specially, $k_1 v$ for the $Ti_2Nb_{10}O_{29}$ electrode is 37.8%, 46.3%, 57.6%, 65.8%, 73.1% and 81.1%. Thus, it can be demonstrated that the pseudocapacitive contributions can be significantly enlarged by decreasing the particle size and decoration of the carbon layer [43, 50].

4 Conclusion

In summary, $Ti_2Nb_{10}O_{29}$/C nanoparticles with good dispersity were synthesized by a simple and effective in situ sol–gel process. A large specific surface area and small grain size can decrease Li^+ diffusion length and offer plenty of accessible active sites for Li^+ storage, leading to a large discharge capacity and superior rate capability. Meanwhile, the carbon layer not only improves the pseudocapacitive effect and electric conductivity, but also serves as an elastic barrier to buffer the stress of the volume change generated in the discharge and charge processes, leading to excellent rate capacity and good cycle performance.

Acknowledgments This study was financially supported by the National Natural Science Foundation of China (No. 51802163), the National Natural Science Foundation of Henan Department of Education (No. 20A480004) and the China Postdoctoral Science Foundation (No. 2017M622564).

References

[1] Yan Z, Yang QW, Wang Q, Ma J. Nitrogen doped porous carbon as excellent dual anodes for Li- and Na-ion batteries. Chin Chem Lett. 2020;31(2):583.
[2] Wang X, Meng Q, Wang Y, Liang H, Bai Z, Wang K, Lou X, Cai B, Yang L. TiO_2 hierarchical hollow microspheres with different size for application as anodes in high-performance lithium storage. Appl Energy. 2016;175:488.
[3] Peled E, Golodnitsky D, Ardel G. Advanced model for solid electrolyte interphase electrodes in liquid and polymer electrolytes. J Electrochem Soc. 1997;144(8):L208.
[4] Hu L, Luo L, Tang L, Lin C, Li R, Chen Y. $Ti_2Nb_{2x}O_{4+5x}$ anode materials for lithium-ion batteries: a comprehensive review. J Mater Chem A. 2018;6(21):9799.
[5] Aravindan V, Sundaramurthy J, Jain A, Kumar PS, Ling WC, Ramakrishna S, Srinivasan MP, Madhavi S. Unveiling $TiNb_2O_7$ as an insertion anode for lithium ion capacitors with high energy and power density. Chem Sus Chem. 2014;7(7):1858.
[6] Lin C, Yu S, Zhao H, Wu S, Wang G, Yu L, Li Y, Zhu JJ, Li J, Lin S. Defective $Ti_2Nb_{10}O_{27.1}$: an advanced anode material for lithium-ion batteries. Sci Rep. 2015;5:17836.
[7] Liao J, Ni W, Wang C, Ma J. Layer-structured niobium oxides and their analogues for advanced hybrid capacitors. Chem Eng J. 2019. https://doi.org/10.1016/j.cej.2019.123489.
[8] Li J, Yang JY, Wang JT, Lu SG. A scalable synthesis of silicon nanoparticles as high-performance anode material for lithium-ion batteries. Rare Met. 2019;36(3):199.
[9] Li J, Liu WW, Zhou HM, Liu ZZ, Chen BR, Sun WJ. Anode material NbO for Li-ion battery and its electrochemical properties. Rare Met. 2018;37(2):118.
[10] Lou S, Cheng X, Gao J, Li Q, Wang L, Cao Y, Ma Y, Zuo P, Gao Y, Du C, Huo H, Yin G. Pseudocapacitive Li^+ intercalation in porous $Ti_2Nb_{10}O_{29}$ nanospheres enables ultra-fast lithium storage. Energy Storage Mater. 2018;11:57.
[11] Tong Z, Xu H, Liu G, Zhao J, Li Y. Pseudocapacitive effect and Li^+ diffusion coefficient in three-dimensionally ordered

macroporous vanadium oxide for energy storage. Electrochem Commun. 2016;69:46.
[12] Li Y, Zheng Y, Yao J, Xiao J, Yang J, Xiao S. Facile synthesis of nanocrystalline-assembled nest-like NiO hollow microspheres with superior lithium storage performance. RSC Adv. 2017; 7(50):31287.
[13] Wang HE, Zhao X, Xin K, Li Y, Chen L, Yang X, Zhang W, Su BL, Cao G. Superior pseudocapacitive lithium-ion storage in porous vanadium oxides@C heterostructure composite. ACS Appl Mater Inter. 2017;9(50):43665.
[14] Lübke M, Shin J, Marchand P, Brett D, Shearing P, Liu Z, Darr JA. Highly pseudocapacitive Nb-doped TiO_2 high power anodes for lithium-ion batteries. J Mater Chem A. 2015;3:22908.
[15] Liu X, Liu M, Hu Y, Hu M, Duan X, Liu G, Ma J. Mesoporous $Ti_2Nb_{10}O_{29}$ microspheres constructed by interconnected nanoparticles as high performance anode material for lithium ion batteries. Ceram Int. 2019;45(3):3574.
[16] Liu G, Jin B, Bao K, Liu Y, Xie H, Hu M, Zhang R, Jiang Q. Facile fabrication of porous $Ti_2Nb_{10}O_{29}$ microspheres for high-rate lithium storage applications. Int J Hydrog Energy. 2017;42(36):22965.
[17] Fu Q, Hou J, Lu R, Lin C, Ma Y, Li J, Chen Y. Electrospun $Ti_2Nb_{10}O_{29}$ hollow nanofibers as high-performance anode materials for lithium-ion batteries. Mater Lett. 2018;214:60.
[18] Cong DP, Kim J, Tran VT, Kim SJ, Jeong SY, Choi JH, Cho CR. Electrochemical behavior of interconnected $Ti_2Nb_{10}O_{29}$ nanoparticles for high-power Li-ion battery anodes. Electrochim Acta. 2017;236:451.
[19] Sun Y, Liu X, Huang F, Li S, Shen Y, Xie A. Spinach juice--derived porous Fe_2O_3/carbon nanorods as superior anodes for lithium-ion batteries. Mater Res Bull. 2017;95:321.
[20] Li H, Zhou H. Enhancing the performances of Li-ion batteries by carbon-coating: present and future. Chem Commun. 2012; 48(9):1201.
[21] Sun J, Teng D, Liu Y, Chi C, Yu Y, Lan J, Yang X. Enhanced lithium storage capability of a dual-phase $Li_4Ti_5O_{12}$-TiO_2-carbon nanofiber anode with interfacial pseudocapacitive effect. RSC Adv. 2014;4:48632.
[22] Liu G, Jin B, Zhang R, Bao K, Xie H, Guo J, Wei M, Jiang Q. Synthesis of $Ti_2Nb_{10}O_{29}$/C composite as an anode material for lithium-ion batteries. Int J Hydrog Energy. 2016;41(33):14807.
[23] Wan G, Yang L, Shi S, Tang Y, Xu X, Wang G. $Ti_2Nb_{10}O_{29}$ microspheres coated with ultrathin N-doped carbon layers by atomic layer deposition for enhanced lithium storage. Chem Commun. 2019;55(4):517.
[24] Liu X, Wang H, Zhang S, Liu G, Xie H, Ma J. Design of well-defined porous $Ti_2Nb_{10}O_{29}$/C microspheres assembled from nanoparticles as anode materials for high-rate lithium ion batteries. Electrochim Acta. 2018;292:759.
[25] Huang SZ, Zhang Q, Yu W, Yang XY, Wang C, Li Y, Su BL. Grain boundaries enriched hierarchically mesoporous MnO/carbon microspheres for superior lithium ion battery anode. Electrochim Acta. 2016;222:561.
[26] Ferrari AC, Robertson J. Interpretation of Raman spectra of disordered and amorphous carbon. Phys Rev B. 2000;61(20): 14095.
[27] Ma C, Zhang W, He YS, Gong Q, Che H, Ma ZF. Carbon coated SnO_2 nanoparticles anchored on CNT as a superior anode material for lithium-ion batteries. Nanoscale. 2016;8:4121.
[28] Yao L, Hou X, Hu S, Wang J, Li M, Su C, Tade MO, Shao Z, Liu X. Green synthesis of mesoporous $ZnFe_2O_4$/C composite microspheres as superior anode materials for lithium-ion batteries. J Power Source. 2014;258:305.
[29] Wang YX, Yang J, Chou SL, Liu HK, Zhang WX, Zhao D, Dou SX. Uniform yolk-shell iron sulfide-carbon nanospheres for superior sodium-iron sulfide batteries. Nature Commun. 2015;6: 8689.
[30] Liu G, Liu X, Wang L, Ma J, Xie H, Ji X, Guo J, Zhang R. Hierarchical $Li_4Ti_5O_{12}$-TiO_2 microspheres assembled from nanoflakes with exposed $Li_4Ti_5O_{12}$ (011) and anatase TiO_2 (001) facets for high-performance lithium-ion batteries. Electrochim Acta. 2016;222:1103.
[31] Liu H, Zhang Z, Hu L, Gao N, Sang L, Liao M, Ma R, Xu F, Fang X. New UV-A photodetector based on individual potassium niobate nanowires with high performance. Adv Opt Mater. 2014;2(8):771.
[32] Tan BJ, Klabunde KJ, Sherwood PMA. Layered cobalt-manganese particles on alumina and silica. J Am Chem Soc. 1991; 113(3):855.
[33] Hou BH, Wang YY, Guo JZ, Ning QL, Xi XT, Pang WL, Cao AM, Wang X, Zhang JP, Wu XL. Pseudocapacitance-boosted ultrafast Na storage in a pie-like FeS@C nanohybrid as an advanced anode material for sodium-ion full batteries. Nanoscale. 2018;10:9218.
[34] Chen Y, Xia H, Lu L, Xue J. Synthesis of porous hollow Fe_3O_4 beads and their applications in lithium ion batteries. J Mater Chem. 2012;22(11):5006.
[35] Roh HK, Kim HK, Kim MS, Kim DH, Chung KY, Roh KC, Kim KB. In-situ synthesis of chemically bonded $NaTi_2(PO_4)_3$/rGO 2D nanocomposite for high-rate sodium-ion batteries. Nano Res. 2016;6:1844.
[36] Kaowphong S, Chumha N, Nimmanpipug P, Kittiwachana S. Nanosized $GdVO_4$ powders synthesized by sol-gel method using different carboxylic acids. Rare Met. 2018;37(7):561.
[37] Jiang ZY, Zhu KR, Lin ZQ, Jin SW, Li G. Structure and Raman scattering of Mg-doped ZnO nanoparticles prepared by sol-gel method. Rare Met. 2018;37(10):881.
[38] Zhu X, Pei L, Zhu R, Yu J, Tang R, Wei F. Preparation and characterization of Sn/La co-doped TiO_2 nanomaterials and their phase transformation and photocatalytic activity. Sci Rep. 2018; 8:12387.
[39] Ouzzine M, Maciá-Agulló JA, Lillo-Ródenas MA, Quijada C, Linares-Solano A. Synthesis of high surface area TiO_2 nanoparticles by mild acid treatment with HCl or HI for photocatalytic propene oxidation. Appl Catal B-Environ. 2014; 154–155:285.
[40] Jiang C, Ichihara M, Honma I, Zhou H. Effect of particle dispersion on high rate performance of nano-sized $Li_4Ti_5O_{12}$ anode. Electrochim Acta. 2007;52(23):6470.
[41] Viet AL, Reddy MV, Jose R, Chowdari BVR, Ramakrishna S. Nanostructured Nb_2O_5 polymorphs by electrospinning for rechargeable lithium batteries. J Phys Chem C. 2010;114(1):664.
[42] Deng S, Luo Z, Liu Y, Lou X, Lin C, Yang C, Zhao H, Zheng P, Sun Z, Li J, Wang N, Wu H. $Ti_2Nb_{10}O_{29-x}$ mesoporous microspheres as promising anode materials for high-performance lithium-ion batteries. J Power Sources. 2017;362:250.
[43] Xiao C, He P, Ren J, Yue M, Huang Y, He X. Walnut-structure Si-G/C materials with high coulombic efficiency for long-life lithium ion batteries. RSC Adv. 2018;8:27580.
[44] Jung BY, Lim HS, Sun YK, Suh KD. Synthesis of Fe_3O_4/C composite microspheres for a high performance lithium-ion battery anode. J Power Sources. 2013;244:177.
[45] Li X, Jiang YZ, Li XK, Jiang HX, Liu JL, Feng J, Lin SB, Guan X. Electrochemical properties of $LiFePO_4$/C composite cathode with different carbon sources. Rare Met. 2018;37(9):743.
[46] Jiao X, Hao Q, Xia X, Yao D, Ouyang Y, Lei W. Boosting long-cycle-life energy storage with holey graphene supported $TiNb_2O_7$ network nanostructure for lithium ion hybrid supercapacitors. J Power Sources. 2018;403:66.
[47] Jo C, Kim Y, Hwang J, Shim J, Chun J, Lee J. Block copolymer directed ordered mesostructured $TiNb_2O_7$ multimetallic oxide

constructed of nanocrystals as high power Li-ion battery anodes. Chem Mater. 2014;26(11):3508.
[48] Sun YG, Sun TQ, Lin XJ, Tao XS, Zhang D, Zeng C, Cao AM, Wan LJ. Facile synthesis of hollow $Ti_2Nb_{10}O_{29}$ microspheres for high-rate anode of Li-ion batteries. Sci China Chem. 2018;61(6):670.
[49] Zhang Z, Li Q, Li Z, Ma J, Li C, Yin L, Gao X. Partially reducing reaction tailored mesoporous 3D carbon coated NiCo-$NiCoO_2$/carbon xerogel hybrids as anode materials for lithium ion battery with enhanced electrochemical performance. Electrochim Acta. 2016;203:117.
[50] Madram AR, Daneshtalab R, Sovizi MR. Effect of Na^+ and K^+ co-doping on the structure and electrochemical behaviors of $LiFePO_4$/C cathode material for lithium-ion batteries. RSC Adv. 2016;6:101477.
[51] Wang GJ, Qu QT, Wang B, Shi Y, Tian S, Wu YP, Holze R. Electrochemical intercalation of lithium ions into LiV_3O_8 in an aqueous electrolyte. J Power Sources. 2009;189:503.
[52] Mao W, Liu K, Guo G, Liu G, Bao K, Guo J, Hu M, Wang W, Li B. Preparation and electrochemical performance of $Ti_2Nb_{10}O_{29}$/Ag composite as anode materials for lithium ion batteries. Electrochim Acta. 2017;253:396.
[53] Ashish AG, Arunkumar P, Babu B, Manikandan P, Sarang S, Shaijumon MM. $TiNb_2O_7$/Graphene hybrid material as high performance anode for lithium-ion batteries. Electrochim Acta. 2015;176:285.
[54] Zhu K, Wang Q, Kim JH, Pesaran AA, Frank AJ. Pseudocapacitive lithium-ion storage in oriented anatase TiO_2 nanotube arrays. J Phys Chem C. 2012;116(22):11895.
[55] Wang J, Polleux J, Lim J, Dunn B. Pseudocapacitive contributions to electrochemical energy storage in TiO_2 (anatase) nanoparticles. J Phys Chem C. 2007;111(40):14925.
[56] Lindström H, Södergren S, Solbrand A, Rensmo H, Hjelm J, Hagfeldt A, Lindquist SE. Li^+ ion insertion in TiO_2 (anatase). 2. Voltammetry on nanoporous films. J Phys Chem B. 1997;101(39):7717.
[57] Yang C, Zhang Y, Lv F, Lin C, Liu Y, Wang K, Feng J, Wang X, Chen Y, Li J, Guo S. Porous $ZrNb_{24}O_{62}$ nanowires with pseudocapacitive behavior achieve high performance lithium-ion storage. J Mater Chem A. 2017;5(42):22297.
[58] Cook JB, Kim HS, Yan Y, Ko JS, Robbennolt S, Dunn B, Tolbert SH. Mesoporous MoS_2 as a transition metal dichalcogenide exhibiting pseudocapacitive Li and Na-ion charge storage. Adv Energy Mater. 2016;6(9):1501937.